Research article

Solar fuels design: Porous cathodes modeling for electrochemical carbon dioxide reduction in aqueous electrolytes

Inês S. Fernandes [a], Duarte Antunes [a], Rodrigo Martins [a], Manuel J. Mendes [a,*], Ana S. Reis-Machado [a,b,**]

[a] i3N/CENIMAT, Department of Materials Science, NOVA School of Science and Technology, CEMOP/UNINOVA, Campus de Caparica, 2829-516 Caparica, Portugal
[b] LAQV, REQUIMTE, Department of Chemistry, NOVA School of Science and Technology, 2829-516 Caparica, Portugal

A B S T R A C T

The reduction of carbon dioxide emissions is crucial to reduce the atmospheric greenhouse effect, fighting climate change and global warming. Electrochemical CO_2 reduction is one of the most promising carbon capture and utilization technologies, that can be powered by solar energy and used to make added-value chemicals and green fuels, providing grid-stability, energy security, and environmental benefits. A two-dimensional finite-elements model for porous electrodes was developed and validated against experimental data, allowing the design and performance improvement of a porous zinc cathode morphology and its operational conditions for an electrolyzer producing syngas via the co-electrolysis of CO_2 and water. Porosity, pore length, fiber geometric shape, inlet pressure, system temperature, and catholyte flow rate were explored, and these parameters were thoroughly tuned by using the smart-search Nelder-Mead's multiparameter optimization algorithm to achieve pronouncedly higher, industrial-relevant current density values than those previously reported, up to 263.6 mA/cm^2 at an applied potential of −1.1 V vs. RHE.

1. Introduction

1.1. Carbon dioxide utilization

The mitigation and reduction of carbon dioxide emissions is vital to reduce the atmospheric greenhouse effect and combat climate change [1,2]. Strategies to achieve this objective are: the use of renewable energy sources; CO_2 Capture and Storage (CCS) technologies [1–3]; and CO_2 Capture and Utilization (CCU) technologies [1,2,4].

The usage of CO_2 includes: reuse without conversion [5,6], conversion into a fuel, or an energy storage vector [7–10], or use as a raw material for the manufacture of added-value chemicals and materials [3]. Within the CCU technologies, in the class of CO_2 transformations into fuels or energy vectors, the conversion processes can be: biochemical, photosynthetic, thermo-catalytic, photo-catalytic, electrochemical (which is the scope of the present work), and photoelectrochemical [1,2,11–16].

Electrochemical CO_2 Reduction (CO$_2$R) is one of the most promising CO_2 utilization technologies, because the electrolyzers allow:

---

* Corresponding author.
** Corresponding author. LAQV, REQUIMTE, Department of Chemistry, NOVA School of Science and Technology, 2829-516 Caparica, Portugal.
E-mail addresses: mj.mendes@fct.unl.pt (M.J. Mendes), ams.machado@fct.unl.pt (A.S. Reis-Machado).

operation under moderate operating conditions (near room temperature and atmospheric pressure); highly controllable selectivity of the reactions' product(s), e.g. by management of the applied potential and/or the current density; and easy modular design for the assembly of large yield reactors [17].

Nevertheless, the overarching sustainability of CO_2R requires powering by renewable electricity, e.g., solar or wind energy [18–20]. In particular, solar-to-fuel technologies are now considered highly promising to mitigate CO_2 emissions in buildings [7,8], transportation, and industries with heavy carbon footprints that can integrate CO_2 recycling [21] in their production processes [3].

However, the economic viability (cost-effectiveness) of the electrochemical CO_2 conversion processes into: CO [22–24], CH_4 [7,8], C_2H_4 [25], alcohols [26], formic acid (HCOOH) [17,27], among other useful hydrocarbons, still needs substantial enhancement to allow their massive deployment. For the time being, most of these technologies are just too expensive to implement on a practical and/or commercial scope, and still require a great deal of R&D efforts [3].

In Fig. 1a, the solar fuels cycle concept is explained in some detail: the CO_2 emitted to the atmosphere, by anthropogenic means, can be captured and utilized (recycled) via CCU technologies, e.g. involving CO_2R electrolyzers for green fuel production. For this, photovoltaic electricity [7,8] and water must be provided to feed the renewable fuels production by electrolysis, which then can be used for commercial, industrial or mobility purposes.

The main challenges, technical and economic, to the implementation of CO_2R as a commercially viable technology, are: the high energy requirements to break down the double-bond of the CO_2 molecule [29]; the low selectivity of the most desired products, which increases costs due to the complexity of their separation processes, since many of the existing CO_2R reactions (excluding the competing Hydrogen Evolution Reaction, HER) have standard equilibrium potentials in the small electric potential range between -0.25 and -0.17 V vs. SHE; the CO_2R kinetic rates are limited by the slow CO_2 mass transfer from the gas phase to the liquid aqueous electrolyte, and to the active sites of the cathode catalysts; the electrocatalysts instability during long operation times, which is caused by the catalyst poisoning with impurities from the electrolyte [30,31], and/or from the CO_2 feed gas [3], as well as from the resulting products of the corrosion of the electrolyzer components [32–38].

To circumvent these issues, the proposed approaches go through the performance improvement of the device design and the operating conditions parameters, namely: the electrolyzer configuration, the electrodes' structures, the electrolyte selection, the electrolyte pH, the inlet and the outlet pressures, the electrochemical cell compartments temperatures, and especially, the catalysts materials and composition [3].

The main challenge in CO_2 electrolyzers design is ensuring sufficient CO_2 delivery to the cathode surface. This aspect can be limited by the CO_2's low solubility at ambient conditions or its slow mobility in aqueous electrolytes. Gas diffusion electrodes (GDEs) can solve this by providing CO_2 in the gas phase behind the electrode [39–41], addressing mobility. Alternatively, concentration can be increased by using non-aqueous solvents [42–44] or applying high pressures [42,45,46]. GDEs offer faster CO_2 delivery but require a multi-component complex structure, while the use of liquid phase electrodes in a system with increased CO_2 solubility allows simplifying the electrode design. The use of CO_2 inlet pressures higher than atmospheric pressure was the strategy followed in the present work to address this issue. Further information on GDEs modeling and detailed descriptions of their features can be found in Heβelmann et al. [47], El-Shafie et al. [48], Morrison et al. [49], and other relevant works [50–57].
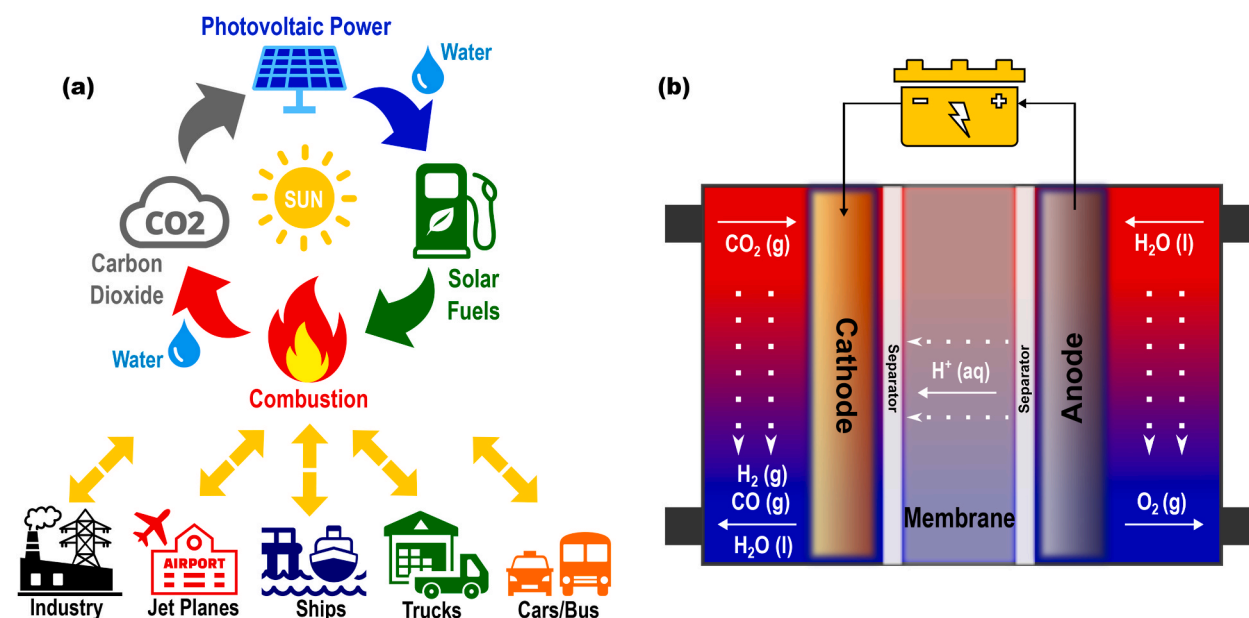

Fig. 1. (a) Schematic of the solar fuels concept. Inspired by Ref. [28]. (b) Scheme of a Membrane-Electrode-Assembly (MEA) electrolyzer, representative of an electrochemical CO_2 reduction (CO_2R) and water-splitting electrolytic system with a zero-gap configuration. Components not at scale. Adapted from Ref. [9].

The need for the electrodes' design enhancement, and a better understanding of the electrolyte chemical species concentration profiles and transport kinetics, go hand in hand with the development of advanced manufacturing technologies, such as 3D printing [58], which can greatly benefit from theoretical guidance given by computational modeling studies, to maximize the improvement of the electrodes morphologies, and of the electrolyzers' components arrays and respective dimensions [3].

Although CO_2R facilities are already operating at pilot scale, e.g. with current densities on the order of 100–200 mA/cm^2 [3] using GDEs, there is still a considerable lack of literature developments reporting on practical simulation tools capable of accurately modeling and boosting the performance of such devices via comprehensive, low-resource demanding and adaptative computational methods.

For instance, GDEs are composite layered structures prone to delamination issues and catalyst instability, while free-standing three-dimensional porous electrodes have the potential to overcome these problems. Nonetheless, from an experimental standpoint, it is particularly difficult to determine the characteristics of the species' transport inside the porous structures. This is an example of a key aspect in which modeling can help to understand the influence of electrode morphology and operation conditions in CO_2R.

Intensive efforts are being undertaken to advance modeling in the electrochemical reduction of CO_2. Methods that employ density functional theory (DFT) establishing linear-scaling relationships have allowed some rational understanding of activity volcano plots [59,60]. It is now often employed to estimate the information needed in mechanistic studies. DFT and micro-kinetic modeling – micro modeling approaches – have been recently reviewed elsewhere [61]. However, this methodology is limited to a family of materials, in general to metals and does not encompass the complexity of whole phases and catalyst/support interactions. Thus, nowadays efforts are directed to circumvent the linear scaling relationships [62].

Besides Faradaic processes, phenomena occurring in the diffusion layer are of the utmost importance to enhance CO_2R. The multiphysic modeling approach is very suitable to deal with this challenge. Kas et al. [57] modeled CO_2 reduction on a GDE with an Ag catalyst layer. The 2D model accounted for Butler-Volmer kinetics for both CO_2R and H_2O, as well as CO_2/bicarbonate/carbonate equilibria reactions within the electrolyte. As a main result, the interdependence of applied potential, current density, and outlet concentrations was disclosed. Singh et al. [63] employed a 1D mathematical model for an electrochemical cell for CO_2R with anolyte, catholyte, Pt anode, Cu and Ag cathode, and an anion-exchange membrane. COMSOL Multiphysics® software was used to solve the model including ion migration, diffusion, acid-base equilibrium, gas-liquid transport of CO_2, hydrolysis of cations, and kinetics for both Oxygen Evolution Reaction (OER) and CO_2. This model allowed to understand the cation effect in the CO_2R and suggested that weakly hydrated cations have a lower pK_a (negative base-10 logarithm of the acid dissociation constant, K_a, of a solution, which means that stronger acids have lower pK_a values) at the surface, thus they allow for an increased pH buffering and higher CO_2 availability while achieving an excellent agreement with experimental results. Multiphysics 3D modeling by Veenstra et al. [64] is another successful application of the multiphysics framework. Combining computational estimations with experimental results for CO_2R selectivity, maps for different reaction products were created, highlighting the role of surface pH and average CO_2 concentration at the electrode in reaction selectivity.

This work addresses for the first time an unprecedented modeling methodology capable of fully describing the operation of porous electrodes and tuning their morphology for the performance improvement of CO_2R cathodes with industrially attractive performances. Specific objectives are the maximization of current density, productivity, and consequently, energy efficiency. To achieve this, the smart-search Nelder-Mead's optimization algorithm was used to fine-tune and improve the performance of a system by adjusting up to four parameters simultaneously. In this way, we aimed to achieve the best possible cathode configuration for experimental realization in subsequent works.

1.2. Carbon dioxide electroreduction mechanism

A CO_2 electrolyzer consists of: a cathode to reduce CO_2 into products such as CO, or HCOOH/HCOO$^-$, and to produce hydrogen; an anode to oxidize water via the OER, generating protons (H$^+$) and electrons (e$^-$); an electrolyte to conduct ions, and to dissolve and transport CO_2 to the cathode active sites; an ion exchange membrane, or a porous diaphragm, to separate the cathode from the anode; and a voltage source, with sufficient applied (electric) potential to transfer electrons from the anode to the cathode.

Fig. 1b depicts a membrane-electrode-assembly (MEA) electrolytic cell which performs CO_2R and water splitting to produce gaseous CO and H$_2$ (syngas components). The electrolyzer design analyzed in this work is taken to be composed of a Zn porous cathode, a commercial metallic anode, a protonic exchange membrane, two porous separator diaphragms, catholyte/anolyte chambers with inlet and outlet, and a power source to apply the electric potential driving the reaction.

In such an electrochemical system, there are seven key steps involved in the CO_2R process: (1) transfer of CO_2 from the gaseous phase to the liquid aqueous electrolyte; (2) transport of dissolved CO_2 and protons (H$^+$) from the bulk of the electrolyte to the cathode/electrolyte interface; (3) adsorption of chemical species, such as CO_2, or protons (H$^+$), on the active sites of the cathode surface; (4) dissociation of adsorbed CO_2-like chemical species into intermediate species, such as *COOH, *CO, *CHO, and *COH; (5) transfer of electrons (e$^-$) from the cathode catalyst active sites to the above mentioned intermediate species; (6) desorption of the CO_2R products from the active sites of the negative electrode surface; and (7) migration of the CO_2R products away from the cathode/electrolyte interface into the bulk of the electrolyte again, in gaseous or liquid phases ready for final purification/extraction.

Based on the previously proposed reaction mechanisms of the CO_2-to-CO electrochemical reduction reaction [65,66], the four elementary steps of the reaction (Eqs. (1)–(4)) are as follows ("*" represents an adsorption site):

$$*CO_2 + e^- \rightarrow *CO_2^{\bullet-} \tag{1}$$

$$*CO_2^{\bullet-} + H^+(aq) \rightarrow \ *COOH \tag{2}$$

$$*COOH + H^+(aq) + e^- \rightarrow \ *CO + H_2O(l) \tag{3}$$

$$*CO \rightarrow CO(g) + * \tag{4}$$

Considering the sum of the sequence of reactional steps in Eqs. (1)–(4), the general electrochemical CO2R reaction (Eq. (5)) is:

$$CO_2(g) + 2H^+(aq) + 2e^- \rightarrow CO(g) + H_2O(l) \tag{5}$$

The reduction of the protons (H^+) occurring on that same surface (in an acidic electrolyte) (Eq. (6)) is given by the following reaction:

$$2H^+(aq) + 2e^- \rightarrow H_2(g) \tag{6}$$

The reduction of CO2-to-CO thus involves two electrons and two protons, whose reaction kinetic rate is strongly influenced by the nature of the catalyst (e.g. type of metallic surface, its oxidation state and crystalline structure) [10,65–68]. Therefore, the complete material characterization of the electrocatalyst is an essential input for the understanding of the CO2 kinetic mechanisms.

A key advantage of using free-standing porous electrodes is to achieve a very large active surface area for interaction, without significantly increasing the electrode dimensions, thus improving the electrocatalytic activity. In this work, a zinc-based cathodic material is considered (see Fig. 2a).

The choice of the electrolyte is also critical. Here the electrolyte is taken to be an aqueous solution of 0.1 M KHCO3. In such an electrochemical system, the proton donor is the hydronium cation (H_3O^+, from water H_2O reduction), and not the anion of the supporting electrolyte (HCO_3^-) [69].

Based on a previous contribution by C. Ma et al. [70] which computationally designed electrodes for flow-through batteries, in this work a rigorous two-dimensional numeric model was developed with a finite-elements method (FEM) solver, to allow the design and performance improvement of porous electrodes with arbitrary geometry, for the co-electrolysis of carbon dioxide (CO2) and water (H2O) into syngas (CO + H2).

2. Methodology

The porous cathode FEM model was developed employing the COMSOL Multiphysics® software, via the MUMPS Direct Numerical Method [71], with the following implemented physics interfaces: Secondary Current Distribution; Transport of Diluted Species; and Creeping Flow [70].

The variables inherent to the electrochemical transformations and species transport modules were of quadratic discretization [70], as the software uses FEM to solve partial differential equations by dividing modeling domains into smaller elements, and since shape functions are equations within elements, varying in order and mostly with second order derivative term, then the standard discretization in many cases should be quadratic [72,73].
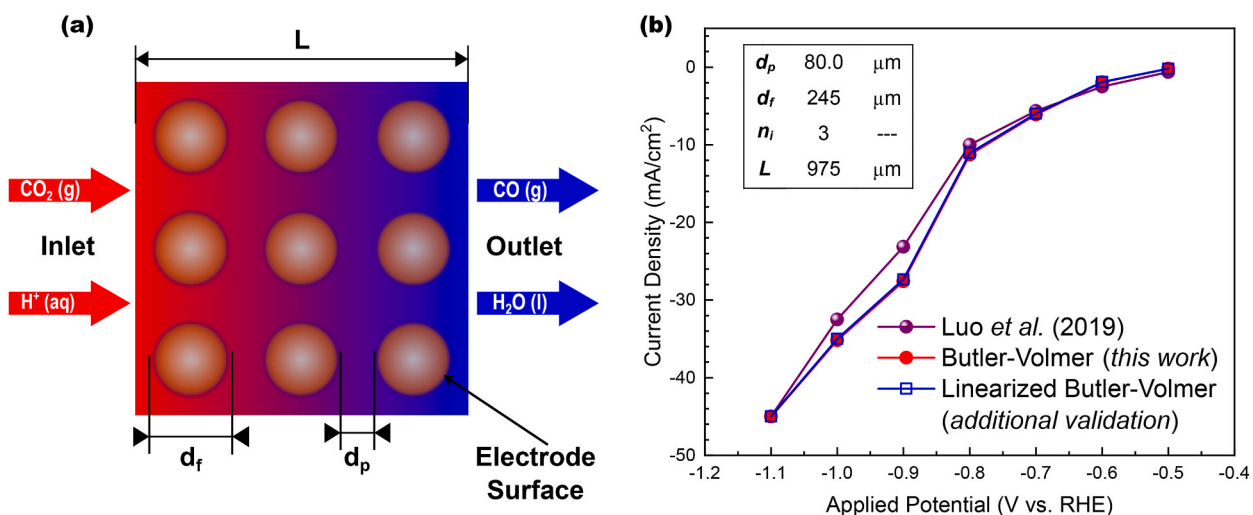
Fig. 2. (a) Two-dimensional porous cathode model design, in which the electrode material comprises infinite cylindrical fibers. The CO2R reaction occurs at the cathode. Inlet and outlet species, along with the main geometric parameters of the electrode, are depicted in the figure: cathode side length, L, fiber diameter, d_f, pore length, d_p, number of fibers per side, n_i (in this example $n_i = 3$, as this is a 3 × 3 fiber arrangement), and electrode surface, S. Adapted from Refs. [69,70]. (b) Comparison between the simulated current-voltage curve [23,24] and the experimentally measured data of the work of Luo et al. [69], employing the validation dimensional parameters indicated in the top-left inset table.

The coupling of the variables that interconnected the modules of the species' transfer mechanisms and of electrochemical processes created modeling situations with highly non-linear processing, whose solutions were quite sensitive to the initial conditions [70]. The Relative Error Tolerance chosen for the porous cathode modeling process was 1×10^{-3}. This value is related to the Solution Termination Criterion of the Segregated Solver method included in the used MUMPS Direct Numerical Method, in the way that the simulation termination depends on the estimated error: it ends when in all the groups of nodes (dependent variables of the implemented physical interfaces), the estimated error in each segregated interaction (the highest estimated damped Newton error) is below the set relative tolerance [74].

The Nelder-Mead Optimization Solver is a COMSOL Multiphysics® tool used to search for the optimum parameter set that maximizes the figure-of-merit (in this case, the CO partial current density, i_{loc}). It is a derivative-free (gradient-free) optimization solver method, that uses a simplex of N+1 points, where N is the total number of control variables that, while not deriving the objective function, enhances the worst point in the simplex during an iteration using reflections, expansions, and contractions [75]. Besides, its software implementation provides a restart method if the simplex form degenerates (i.e., collapses along a direction), its solution also appropriately limits the interval of reflections to obey lower and upper boundaries in the control variable space [76].

2.1. Model geometry

The particular multi-module coupling nature of the COMSOL Multiphysics® software, combining a theoretical mathematical interface of various physical sciences with a 3D designing interface of parts or complete assemblies, allows the complete integration of the geometry of a device into a simulation considering different physical effects occurring simultaneously, all tuned to work together mimicking a real experimental setup.

In the present study, a porous cathode 2D model was implemented whose geometry is set by three parameters: the cathode side length, L, the number of fibers per side, n_i, and the porosity, ε; which are directly related to the design dimensions depicted in Fig. 2a: pore length, d_p, fiber diameter, d_f, total fibers number, N, and superficial fiber area, also named electrode surface, S; according to Eqs. (7)–(10):

$$d_p = \frac{L}{n_i} - d_f \tag{7}$$

$$d_f = \sqrt{\frac{1 - \varepsilon}{\frac{\pi}{4}\frac{N}{L^2}}} \tag{8}$$

$$N = n_i^2 \tag{9}$$

$$S = d_f \times N \times \pi \tag{10}$$

In Fig. 2a, the 2D geometry of the porous cathode model design can be analyzed in detail. To help readers understand the image, the following description is given: the brown circles represent isotropic rigid fibers that are roughly circular in shape (for geometric simplification of the 2D cross-sectional of infinite cylindrical fibers). These fibers make up the solid phase of the electrode. The space between the circles, which is characterized by a color gradient from red to blue, represents the porous space where the liquid phase of the electrode, known as the electrolyte, flows under pressure in the Stokes regime [77,78].

2.2. Model assumptions and limitations

Fluid dynamics, chemical species transport phenomena and electrochemical reactions in aqueous media were combined, which results in a model with non-linear variables and partial differential equations, that accounts for the convection, migration, and diffusion of the charged species responsible for the operation of the porous cathode.

To ease the implementation of this system in the numerical software, reasonable assumptions regarding the transport of charged chemical species were made: the cathode fibers were isotropic and homogeneous; the electrolyte was a Stokes Fluid (creeping flow regime, meaning that its Reynolds Number is substantially below 1, which applies especially to porous domains) [78], an incompressible, isothermal fluid flow and a diluted aqueous solution; no gravity effects; the process worked in stationary state (time-dependent effects are neglected); no clogging (complete connection of the inlet-to-outlet channels with no fluid stagnation between them).

Another geometrical simplification of the computational model concerns its 2D dimensionality, approximating the real (mostly irregular) cathode's fiber structures by regular 2D cross-sectional shapes, in order to minimize the computational demands and allow a better theoretical understanding/interpretation of the main effects at play.

2.3. Mathematical model development

2.3.1. Fluid flow

The description of the fluid flux of a 2D laminar flow regime and the pressure drop was given by the Navier-Stokes Eqs. (11) and (12):

$$\nabla u = 0 \tag{11}$$

$$(u\nabla)\, u + \frac{1}{\rho}\nabla p - \nu\, \nabla^2 u = 0 \tag{12}$$

In Eqs. (11) and (12), the fluid surface velocity vector is u (m/s), the electrolyte density is ρ (kg/m^3), the pressure is p (Pa), and the dynamic fluid viscosity is ν (m^2/s).

2.3.2. Species transport

The conservation equations of chemical species and electric charge in the electrolyte (Eq. (13)) for this model are:

$$- D_i\, \nabla^2 c_i - \nabla\left(\frac{D_i\, z_i\, c_i}{R\, T}\right)\nabla\varphi + u\nabla c_i = 0 \tag{13}$$

In Eq. (13), the concentration of species i is c_i (mol/m^3), the electric charge number of species i is z_i, the diffusion coefficient of species i is D_i (m^2/s), the ionic electric potential is Φ (V vs. RHE), the molar gas constant is $R = 8.3145$ J/(mol.K), and the temperature is T (K).

2.3.3. Electrochemistry

The electrolyte electrical neutrality (Eq. (14)) is described by:

$$\sum_i z_i\, c_i = 0 \tag{14}$$

The balance of electric charge, which is equal to the derivative of the (total) net current density, i (A/m^2), (Eq. (15)), accounts for the variations of the inlet of electrolyte current density, i_l (A/m^2), and of the outlet electrode current density, i_s (A/m^2), considered in this model as follows:

$$\nabla i = \nabla i_l + \nabla i_s \tag{15}$$

The electrolyte current density (Eq. (16)) and electric conductivity, σ_l (S/m), (Eq. (17)), are given by:

$$i_l = F \sum_{i=1}^{n} z_i\big(- D_i - \sigma_l \nabla \varphi_l\big) \tag{16}$$

$$\sigma_l = \frac{F^2}{R\, T} \sum_{i=1}^{n} z_i^2 D_i\, c_i \tag{17}$$

In Eqs. (16) and (17), the Faraday's constant is $F = 9.6485 \times 10^4$ C/mol, and the electrolyte electric potential is Φ_l (V vs. RHE).

Ohm's Law was applied to the electrolyte electric potential (Eq. (18)) and the electrode electric potential, Φ_s (V vs. RHE), (Eq. (19)):

$$i_l = -\sigma_l \nabla \varphi_l \tag{18}$$

$$i_s = -\sigma_s \nabla \varphi_s \tag{19}$$

In Eq. (19), the electrode current density is i_s (A/m^2), and the electrode electric conductivity, σ_s (S/m).

The Nernst equation was used on the porous cathode surface to determine the equilibrium potential of the governing electrochemical CO$_2$R reaction (Eq. (20)), given by:

$$E_{eq} = E_0 + \frac{R\, T}{ne\, F} \ln\left(\frac{a_{CO_2}}{a_{CO}}\right) \tag{20}$$

In Eq. (20), the chemical activity of species i is a_i, which is equal to the dimensionless value of the concentration of species i, or c_i (mol/m^3), the CO$_2$R equilibrium potential is E_{eq} (V vs. RHE), the CO$_2$R standard equilibrium potential is E_0 (V vs. RHE), and the number of electrons transferred during the electrochemical reaction is ne.

The overpotential, η (V vs. RHE), of the CO$_2$R reaction on the porous cathode surface (Eq. (21)), is defined by:

$$\eta = \varphi_s - E_{eq} \tag{21}$$

The (local) transfer current density, i_{loc} (mA/cm^2), was calculated by the Butler-Volmer equation, which was used to define the electrochemical reaction (CO$_2$R) that happens on the porous cathode surface (Eq. (22)), being given by:

$$i_{loc} = i_0 \left\{ a_{CO}\, exp\left[\frac{\alpha_a\, ne\, F\, \eta}{R\, T}\right] - a_{CO_2}\, exp\left(\frac{\alpha_c\, ne\, F\, \eta}{R\, T}\right) \right\} \tag{22}$$

In Eq. (22), the CO$_2$R cathodic transfer coefficient is α_c, and the reaction anodic transfer coefficient is α_a.

The electrochemical constants and the operational parameters used in the simulations of this work are presented in Table 1.

2.3.4. Boundary conditions

As the model assumes a stationary state, a null species transport molar flow, N_i (mol/s), was imposed on the top and bottom outward normal unit vector, $\vec{n}$ (m/s), of the cathode, which translated into two concentration/flux symmetry conditions established at the aforementioned geometric boundaries, resulting in a vertical symmetry of the species concentration flux distribution (Eq. (23)), according to the condition:

$$N_i \; \vec{n} = 0 \begin{cases} 0 \leq x \leq L, y = 0 \\ 0 \leq x \leq L, y = L \end{cases} \tag{23}$$

The following Neumann condition, responsible for regulating the pressure of the porous cathode (Eq. (24)), was applied to all limits of the integration domain, except for the inlet and outlet boundaries:

$$\nabla p \; \vec{n} = 0 \tag{24}$$

The inlet boundary was defined by considering that the species enter with their solution initial concentration at inlet, $c_{i,0}$ (mol/m³), (Eq. (25)), and with the inlet velocity, or the inlet pressure, P_{in} (Pa), (Eq. (26)), which is determined by the flow rate of the chosen pump:

$$c_i = c_{i,0} \tag{25}$$

$$p = P_{in} \tag{26}$$

The outlet boundary was defined according to the outward normal unit vector of the species concentration (Eq. (27)) and by setting a volumetric flow rate, q (m³/s), equal to the catholyte volumetric outflow rate, Q_{out} (m³/s), from the porous cathode compartment (Eq. (28)):

$$- \vec{n} \, D_i \nabla c_i = 0 \tag{27}$$

$$q = Q_{out} \tag{28}$$

Since the present study focuses on the cathode, the model was only applied to the cathodic half-cell. The cathodic current collector was implemented on top of the porous cathode, and the applied electric potential, E_c (A/m²), was swept on the surface of the cathode fibers (Eq. (29)); thus, at the fibers/electrolyte interfaces we establish:

$$\varphi_s = E_c \tag{29}$$

The full porous cathode model has been validated against reference experimental results. The current-voltage curves obtained from the simulation were compared with experimentally measured data from Luo et al. [69], and the results are shown in Fig. 2b, considering the Butler-Volmer formalism (Eq. (22)), which was employed to describe the electrochemical processes presented in this work, as well as the Linearized Butler-Volmer formalism (Eq. S1 in Supplementary Information) which is a simplified case of the former equation that was also tested for comparison and as an additional model validation diagnostic [82]. The details of the validation process, including information on the geometric dimensions and operational conditions, are available in section S1 of Supplementary Information.

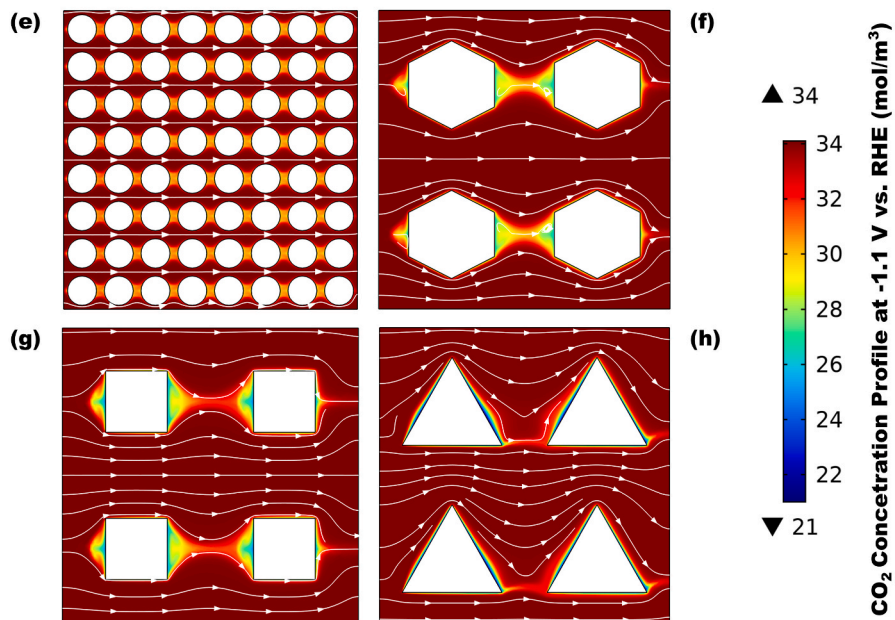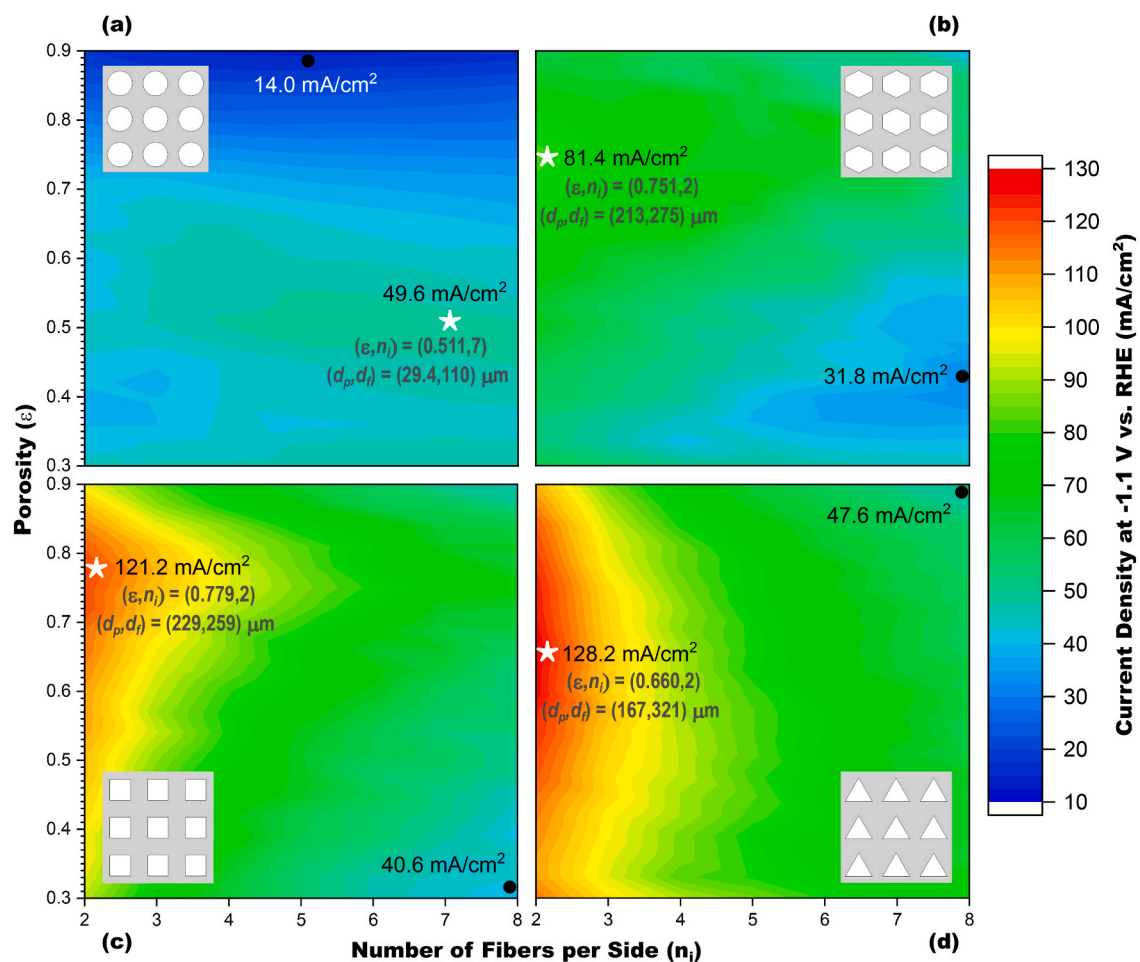## 3. Results and discussion

3.1. Catalyst Fiber Morphology

We start by looking at the effects of two of the main geometric parameters of the porous cathode model: the electrode porosity, ε, and the number of fibers per side, n_i; connected to the design dimensions of Fig. 2a via Eqs. (7)–(10).

For this purpose, three different analyses were conducted to determine the preferential dimensions, all yielding similar findings: (1) maximum current density, i_{loc}, contour plots as a function of n_i and ε, at a set applied electric potential, E_c; (2) Multi-parameter Nelder-Mead Optimization Solver tool, used to smartly search for the i_{loc} maxima, at a determined E_c, by iterative variation of the porous

Table 1
CO₂R species transport and electrochemical parameters. NTP is defined as Normal Temperature and Pressure.

Designation	Symbol	Value	Units	Source
Electrode Conductivity	σ_s	16.6×10^6	S/m	[79]
CO₂R Standard Equilibrium Potential (vs. RHE)	E_0	−0.10	V	[41,80]
CO₂R Exchange Current Density	i_0	8.7488	mA/cm²	[69]
CO₂R Cathodic Transfer Coefficient	α_c	0.5	–	[81]
CO₂R Anodic Transfer Coefficient	α_a	0.5	–	[81]
Electrolyte Density	ρ	1000	g/L	[81]
Electrolyte Kinematic Viscosity	μ	600	g/(cm.min)	[81]
Reference Temperature	T_{ref}	25.0	°C	NTP
Reference Pressure	P_{ref}	1.0133	bar	NTP

(a)

14.0 mA/cm^2

49.6 mA/cm^2

$(\varepsilon, n_l) = (0.511, 7)$
$(d_p, d_f) = (29.4, 110)$ μm

(b)

81.4 mA/cm^2
$(\varepsilon, n_l) = (0.751, 2)$
$(d_p, d_f) = (213, 275)$ μm

31.8 mA/cm^2

(c)

121.2 mA/cm^2
$(\varepsilon, n_l) = (0.779, 2)$
$(d_p, d_f) = (229, 259)$ μm

40.6 mA/cm^2

(d)

47.6 mA/cm^2

128.2 mA/cm^2
$(\varepsilon, n_l) = (0.660, 2)$
$(d_p, d_f) = (167, 321)$ μm

Porosity (ε)

Number of Fibers per Side (n$_i$)

Current Density at -1.1 V vs. RHE (mA/cm^2)

(e)

(f)

(g)

(h)

▲ 34

CO$_2$ Concetration Profile at -1.1 V vs. RHE (mol/m^3)
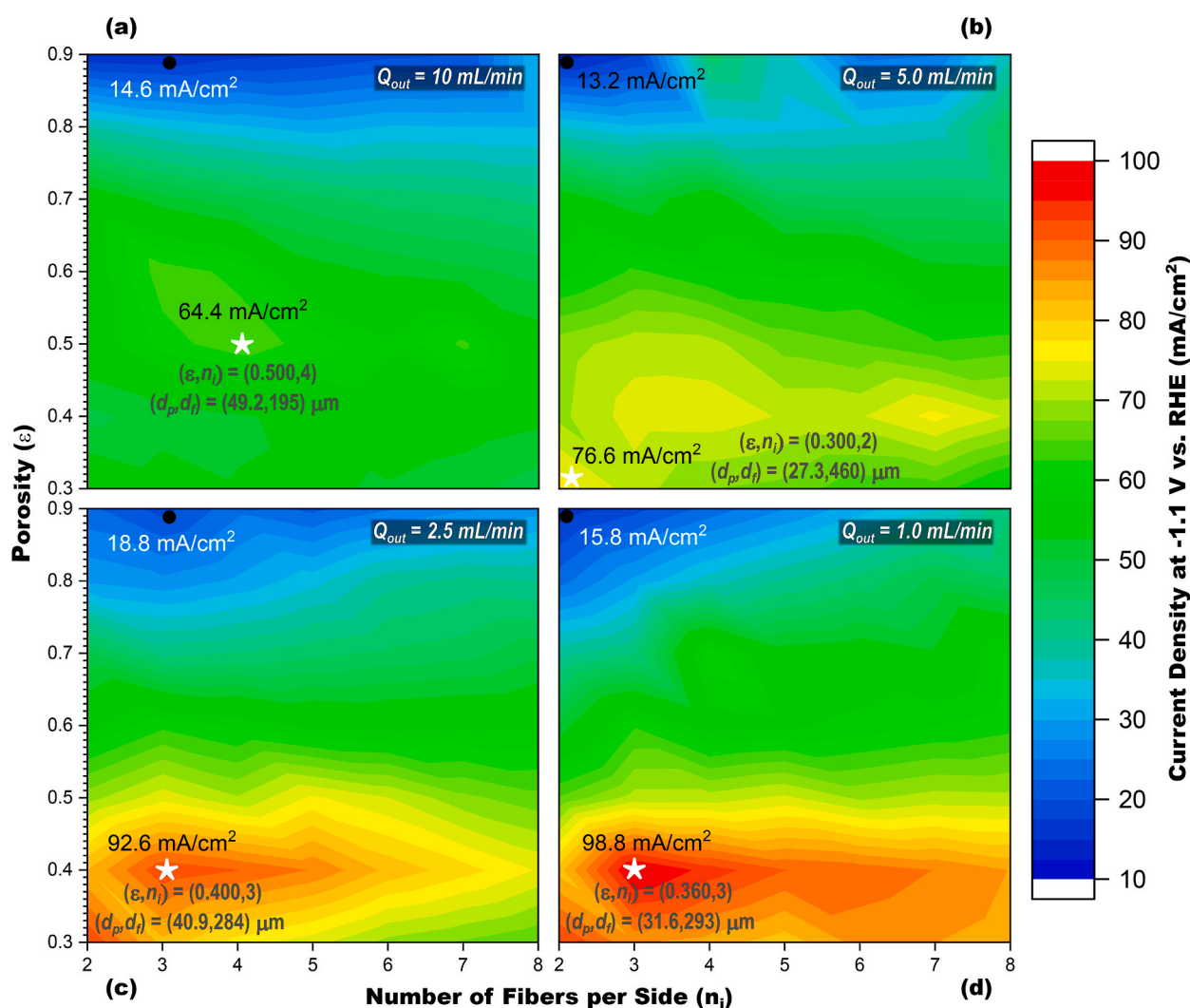
▼ 21

(caption on next page)

Fig. 3. Contour plots of the current density i_{loc} as a function of number of fibers per side n_i vs. cathode porosity ε (a–d), and CO_2 solution concentration profiles of the best cases (e–h), with the respective species total flux streamlines, for different fibers geometric shapes (shown in the corners of the top contour plots): (a, e) circle, (b, f) regular hexagon, (c, g) square, and (d, h) equilateral triangle. The fixed operating parameters implemented were: $E_c = -1.1$ V vs. RHE, $T = 21.85$ °C, $P_{in} = 1.0133$ bar, and $Q_{out} = 21$ mL/min. Captions: Pore Length, d_p; Fiber Diameter, d_f; Applied Electric Potential, E_c; Operating Temperature, T; Inlet Pressure, P_{in}; Volumetric Outflow Rate, Q_{out}; White Star symbol, maxima i_{loc} of each contour plot; and Black Dot symbol, minima i_{loc} of each contour plot.

cathode parameters; and (3) polarization curves as a function of n_i, ε, and fiber geometric shape variation, with the E_c range of -1.5 to -0.5 V vs. RHE. The latter results are not presented in the main manuscript since they yielded similar outcomes as the ones from analysis (2) but are shown in section S2 of Supplementary Information, and the final trends of the three types of analyses are compared in Section 4.

The contour plots obtained via the analysis (1) are depicted in Fig. 3a–d, for an electrolyzer temperature, T, of 21.85 °C, an inlet pressure, P_{in}, of 1.0133 bar and a catholyte flow rate, Q_{out}, of 21 mL/min (model validation operational conditions), at $E_c = -1.1$ V vs. RHE, for the catalyst fibers with different cross-sectional shapes. Fig. 3a shows the case of a circular fiber shape, where the best combination of cathode porosity vs. number of fibers per side was $\varepsilon = 0.511$ with $n_i = 7$ (labelled in the plot), which yielded a maximum $i_{loc} = 49.6$ mA/cm^2 (more than 10% higher than the 45.0 mA/cm^2 obtained by Luo et al. [69] – reference value). A slightly

Fig. 4. Contour plots of the current density i_{loc} as a function of number of fibers per side n_i vs. cathode porosity ε with catholyte flow rates Q_{out} of (a) 10 mL/min, (b) 5.0 mL/min, (c) 2.5 mL/min, and (d) 1.0 mL/min. The fixed operating and morphologic parameters implemented were: $E_c = -1.1$ V vs. RHE, $T = 21.85$ °C, $P_{in} = 1.0133$ bar, and circular fiber shape. Captions: Pore Length, d_p; Fiber Diameter, d_f; Applied Electric Potential, E_c; Operating Temperature, T; Inlet Pressure, P_{in}; White Star symbol, maxima i_{loc} of each contour plot; and Black Dot symbol, minima i_{loc} of each contour plot.

higher result was attained with the Nelder-Mead method, whose best combination of cathode dimensions, at the same E_c, was $\varepsilon = 0.675$ with $n_i = 3$, yielding $i_{loc} = 54.7$ mA/cm^2.

To assess the effect of the fibers' geometric shape on the CO partial current density, i_{loc}, at the chosen $E_c = -1.1$ V vs. RHE, three different 2D cross sections with regular shapes were compared (see Fig. 3a–d): a – the circle, mimicking 3D cylindrical fiber geometry; b – the regular hexagon, corresponding to 3D regular-hexagonal-based prismatic geometry; c – the square, corresponding to 3D square-based prismatic geometry; and d – the equilateral triangle, or 3D equilateral-triangular-based prismatic geometry.

When designing the different geometrical shapes, the authors chose to keep the surface area, S (mm^2), constant, to allow a meaningful comparison between the electrochemical performances of the different porous cathode designs.

Fig. 3a–d shows that, when moving from circular to polyhedral fibers, the optimal parameters and maximum attainable current densities are significantly changed. With regular hexagons (Fig. 3b), the best combination of cathode porosity vs. number of fibers per side is $\varepsilon = 0.751$ with $n_i = 2$, yielding $i_{loc} = 81.4$ mA/cm^2, which is 81% higher than the reference value (45.0 mA/cm^2) of Luo et al. [69]. Reducing the number of fiber sides to squares (Fig. 3c) further increases the maximum $i_{loc} = 121.2$ mA/cm^2 (an increase of about 170% relative to the reference value) at $\varepsilon = 0.779$ with $n_i = 2$. Lastly, with equilateral triangles (Fig. 3d) the highest value of 128.2 mA/cm^2 is achieved (an increase of 185% in comparison with the reference value), with $\varepsilon = 0.660$ and $n_i = 2$.

Whereas with the Nelder-Mead method, the best combinations of cathode design dimensions were: for the circular geometric shape, $\varepsilon = 0.675$ with $n_i = 3$ gained 54.7 mA/cm^2, allowing an enhancement of 22%; for the regular hexagonal geometric shape, $\varepsilon = 0.753$ with $n_i = 2$ developed $i_{loc} = 81.7$ mA/cm^2, providing a higher i_{loc} of 81%; for the square geometric shape, $\varepsilon = 0.769$ with $n_i = 2$ achieved 122.2 mA/cm^2, enabling an increase of 172% of i_{loc} production; and for the equilateral triangular geometric shape, $\varepsilon = 0.753$ with $n_i = 2$ obtained 128.6 mA/cm^2, increasing 186% in comparison to the i_{loc} value at $E_c = -1.1$ V vs. RHE of the reference value.

Fig. 3e–h present the CO_2 solution concentration profiles, c_{CO_2}, of the cases of maximum i_{loc}, for each fiber geometric shape shown in Fig. 3a–d, with the respective species total flux streamlines, for a better understanding of the species transport mechanisms in the electrolyte aqueous solution of the porous cathode. As could be expected, in the simulated i_{loc} values for each fiber shape, the lowest CO_2 concentration on the fiber surface ($c_{CO_2} = 21$ mol/m^3 or mM) corresponds to the highest i_{loc} value obtained (128.2 mA/cm^2), which is the equilateral triangular fiber shape, and the same applies to the relationship of i_{loc} vs. CO_2 concentration on the fiber surface for all the fiber geometric shapes. The trend shows that, as the polyhedral sides of the fiber decrease, the i_{loc} increases. This is linked to the increased disruption of the species' flux streamlines caused by the electrolyte deterrence in the intersections of the fibers, as can be seen in Fig. 3h. Such increased deterrence caused by the fiber geometries with a lower number of polyhedral sides appears to contribute to the higher CO_2 consumption on the fiber surface, thus leading to an increased i_{loc} and consequently an enhancement of the production of the electrochemical system.

3.2. Catholyte flow rate

In this section, the influence of the cathode porosity, ε, the number of fibers per side, n_i, for the circular geometric shape fiber, and the catholyte flow rate, Q_{out}, on current density, i_{loc}, was examined at the applied potential, E_c, of -1.1 vs. RHE.

In Fig. 4a–d the four contour plots, generated from the analysis (1), in the previous conditions of temperature, T, and inlet pressure, P_{in}, are depicted. The figure displays simulated i_{loc} values for catholyte flow rates, with improved performance parameters of $\varepsilon = 0.360$, $n_i = 3$, and $Q_{out} = 1.0$ mL/min, resulting in a 120% increase relative to the reference value. The Nelder-Mead methodology maximizes the i_{loc} value by $\varepsilon = 0.346$ with $n_i = 3$, and $Q_{out} = 1.0$ mL/min, achieving a 171% enhancement.

Examining Fig. 4a–d it is possible to notice high i_{loc} zones (yellow-red regions) at the bottom of the b – d plots. As the Q_{out} decreases, there is a gradual appearance of an improved i_{loc} area around $n_i = 3$ and the ε range of 0.3–0.4, where it is located the maximized i_{loc}. The emergence of such higher-performance zones is likely due to similar reasons as those explained in Section 3.1 for the i_{loc} increase. In the former case the increase in the electrolyte deterrence in the intersections of the fibers was caused by the lower number of polyhedral sides of the geometry of the fibers, while in the present case it is mainly caused by the lower values of Q_{out}, n_i and ε.

Within the prospection range of this analysis there is a trend of increasing i_{loc} maxima with the decrease of Q_{out}. Nevertheless, in practice a maximum in the curve i_{loc} vs. Q_{out}. can be expected, as observed experimentally [9]. For high Q_{out} above the 5.0 mL/min the adsorption of species at the surface of the electrode is not facilitated and the extent of the reaction is decreased, as predicted by the model, while for lower Q_{out} mass transfer limitation effects can occur in real systems which lead to reduced current densities.

3.3. Pressure and temperature

The last study presented herein explored the relationship between cathode porosity, ε, number of fibers per side, n_i, catholyte inlet pressure, P_{in}, and electrolyzer operating temperature, T, for the cathode with circular fiber morphology, and their influence on cathodic current density generation, i_{loc}.

Fig. 5 a – p shows fifteen contour plots created from the analysis (1), for a variable T, and a variable P_{in}, at a fixed catholyte flow rate, Q_{out}, of 21 mL/min (Q_{out} of model validation). This figure depicts the simulated results of the i_{loc}, at $E_c = -1.1$ V vs. RHE, for all the combinations of the following operational parameters: temperatures of 20.0 (Fig. 5a, d, g, j, n), 45.0 (Fig. 5b, e, h, l, o), and 70.0 °C (Fig. 5c, f, i, m, p), and inlet pressures of 1.0 (Fig. 5a–c), 5.0 (Fig. 5d–f), 10.0 (Fig. 5g–i), 15.0 (Fig. 5j–m), and 20.0 bar (Fig. 5n–p).

Based on the survey of the fifteen charts according to their T, the results show that at 20.0 °C, $\varepsilon = 0.700$ with $n_i = 8$ and $P_{in} = 20.0$ bar produced the highest i_{loc} improvement of 177%. Nevertheless, the highest i_{loc} value using the Nelder-Mead method analysis was achieved with $\varepsilon = 0.727$ and $n_i = 7$ at 20.0 bar and 34.0 °C, resulting in an outstanding 486% increase compared to the reference value.

To explain the resulting trends of Fig. 5a–p we first note that these are not justified by the variation of the diffusion coefficient of
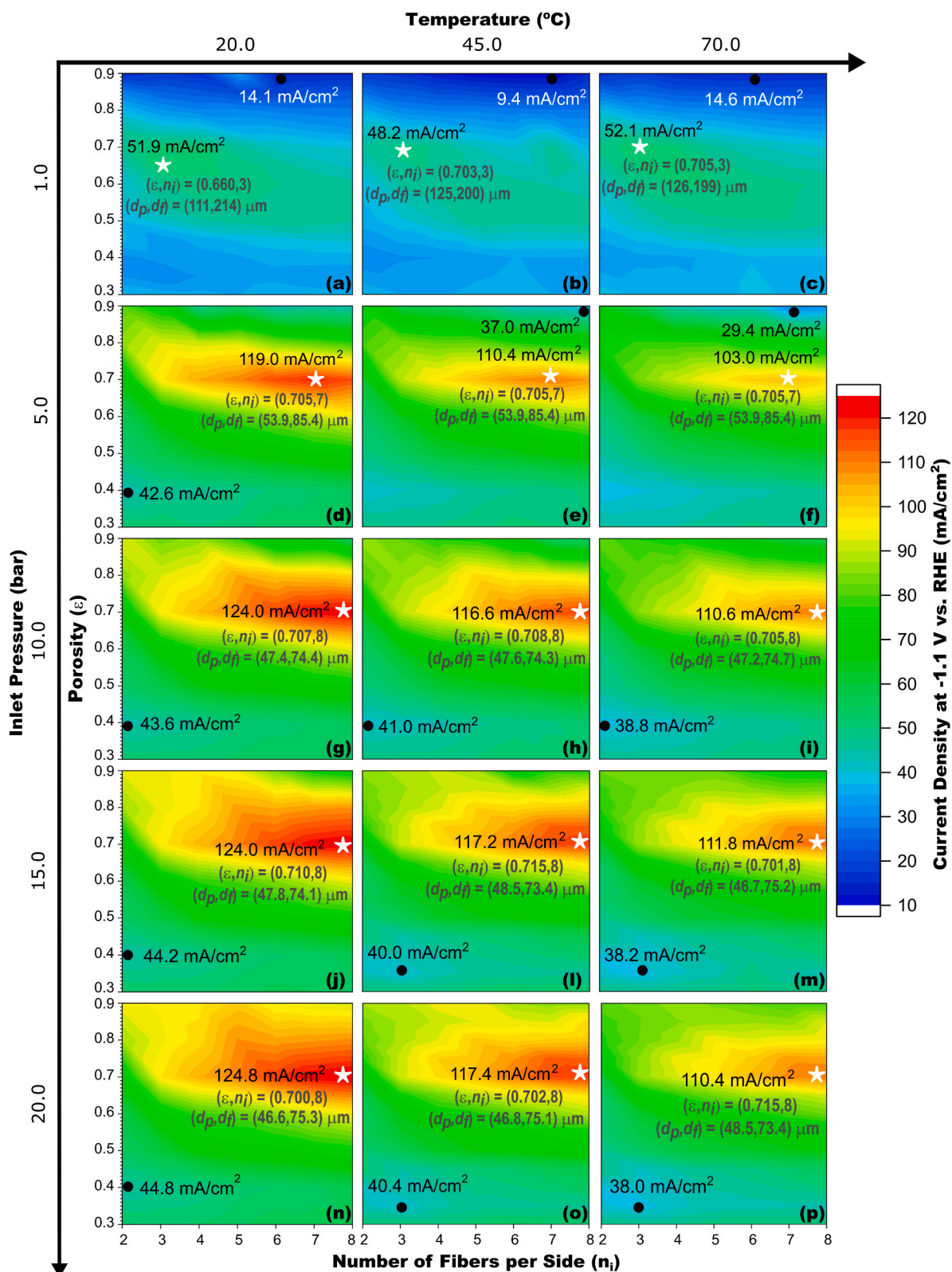
(caption on next page)

Fig. 5. Contour plots of the current density i_{loc} as a function of number of fibers per side n_i vs. cathode porosity ε with catholyte inlet pressures P_{in} of (a–c) 1.0, (d–f) 5.0, (g–i) 10.0, (j–m) 15.0, and (n–p) 20.0 bar, and with cathodic half-cell temperatures T of (a, d, g, j, n) 20.0, (b, e, h, l, o) 45.0, and (c, f, i, m, p) 70.0 °C. The fixed operating and morphologic parameters implemented were: $E_c = -1.1$ V vs. RHE, $Q_{out} = 21$ mL/min, and circular fiber shape. Captions: Pore Length, d_p; Fiber Diameter, d_f; Applied Electric Potential, E_c; Volumetric Outflow Rate, Q_{out}; White Star symbol, maxima i_{loc} of each contour plot; and Black Dot symbol, minima i_{loc} of each contour plot.

CO$_2$, D_{CO_2}. Higher values of D_{CO_2} improve the transport of species, but this quantity generally decreases with P_{in} and increases with T for gaseous species in aqueous solutions [83], so it can be observed that it is not the dominant mechanism dictating the T and P_{in} dependence of the present CO$_2$R process.

The enhancement of the i_{loc} values with the increase in P_{in} is chiefly due to the increase of the CO$_2$ solubility in the electrolyte, which consequently improves the availability of CO$_2$ at the electrode surface for the reaction [2]. Increasing the temperature raises the reaction rate, but as the solubility of CO$_2$ decreases with temperature there will be an optimum temperature to carry out the reaction. In fact, it was verified that the CO$_2$ solubility, which is considered in the simulation as the CO$_2$ initial concentration, $c_{CO_2,0}$, dissolved in the KHCO$_3$ aqueous solution inlet, only increases with decreasing T when $P_{in} < 300.0$ bar and $T < 65$ °C [84]. The results of the simulation undertaken in the present work show a maximum at 34.0 °C and 20.0 bar.

4. Conclusions

Electrochemical CO$_2$ reduction is a complex dynamic process involving many inter-related parameters and effects at play, as cathode surface changes, effect of electric field, electrolyte, adsorption of species, mass transfer, and effects of surface and bulk pH. Numeric mesh-based multiphysics models represent a good approach to describe and integrate all these phenomena.

A two-dimensional finite-elements model for porous zinc electrodes was developed, validated, and corroborated to design and enhance the performance of porous cathodes in CO$_2$ reduction electrolyzers. The following conclusions were drawn:

- The assessment of polarization curves, contour plot analysis and the smart-search Nelder-Mead optimization algorithm, while considering the joint influence of cathode porosity, the number of fibers per side, and fiber cross-sectional shapes, revealed the conditions to allow a 186% enhancement compared to the experimental results used for model validation (depicted in Fig. 6 a, b by the darkest blue column).
- Examining the catholyte flow rate (consideration only circular fibers for simplicity) resulted in 171% increase in cathodic current density compared to the experimental results, achieved by fine-tuning the flow rate to the minimum value studied (1.0 mL/min).
- Analyzing the impact of increased inlet pressure and system temperature (for circular-shaped fibers only) yielded a notable 486% increase in current density (263.6 mA/cm^2 at -1.1 V vs. RHE, denoted by the red column in Fig. 6 a, b). This enhancement was
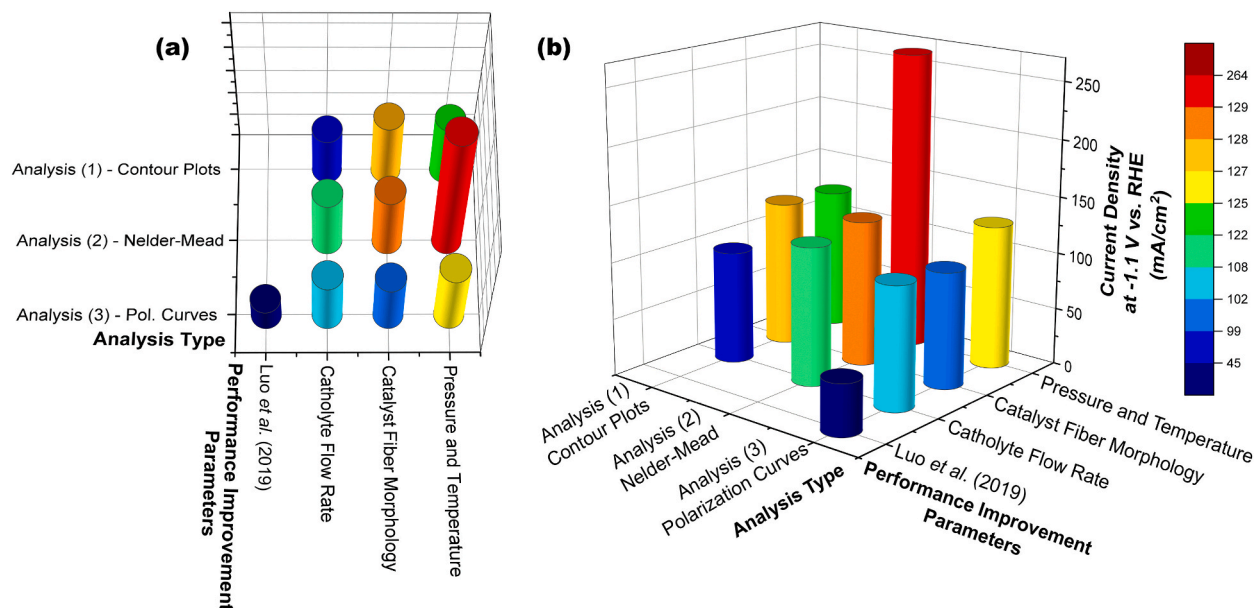
Fig. 6. (a) Top view and (b) orthogonal view of the best-simulated results of the current density at -1.1 V vs. RHE obtained by the porous cathode model for each analysis type: Analysis (1) – Contour Plots, Analysis (2) – Nelder-Mead algorithm, Analysis (3) – Polarization Curves (see section S2 of Supplementary Information); and for each class of performance improvement study: Catholyte Flow Rate, Catalyst Fiber Morphology, and Pressure and Temperature; in comparison with the experimental validation data of Luo et al. [69].

achieved by adjusting the temperature to 34.0 °C and the pressure to 20.0 bar, revealing the significance of identifying the optimal pressure and temperature balance for intensifying the CO_2 reduction process.

Thus, this study indicates that the 2D computational design of free-standing porous cathodes shows great potential for advancing CO_2 electroreduction technology.

4.1. Final perspectives

The production of CO from CO_2 electroreduction can be increased by applying useful recommendations deduced from the use of the 2D model of zinc porous cathodes described in this work, coupled with smart-search optimization algorithms and the parametric study of the fluid dynamics and its main geometric and operational parameters.

A learning-loop should be established between modeling previsions and guidance from catalyst preparation and treatment methods. The development of advanced *in situ* characterization methods, such as Operando Electrochemical Scanning Tunneling Microscopy (EC – STM), Attenuated Total Reflectance Surface-Enhanced Infrared Absorption Spectroscopy (ATR – SEIRAS) and *in situ* Atomic Force Microscopy allow to refine the models and improve their predictive power, bringing new insights for the development of breakthrough catalytic electrodes. Although still in its infancy, in what concerns applications in electrochemical CO_2 reduction, machine-learning offers enormous potential in computational modeling and significant efforts are still needed to realize its full potential. The information provided by advanced modeling raises the bar for the synthesis of new materials. Breakthroughs in fabrication processes and materials treatment, such as laser ablation, laser activation, additive manufacturing, etc., are necessary towards enhanced synthesis resolution and accuracy.

Data availability statement

Data associated with the study has not been deposited into a publicly available repository. Data will be made available on request.

CRediT authorship contribution statement

Inês S. Fernandes: Writing – review & editing, Writing – original draft, Validation, Software, Methodology, Investigation, Conceptualization. **Duarte Antunes:** Writing – original draft, Validation, Software, Methodology, Investigation. **Rodrigo Martins:** Writing – review & editing, Supervision, Project administration, Funding acquisition. **Manuel J. Mendes:** Writing – review & editing, Supervision, Project administration, Methodology, Funding acquisition, Conceptualization. **Ana S. Reis-Machado:** Writing – review & editing, Supervision, Project administration, Funding acquisition, Conceptualization.

Declaration of competing interest

The authors declare that they have no known competing financial interests or personal relationships that could have appeared to influence the work reported in this paper.

Acknowledgements

Appendix A. Supplementary data

Supplementary data to this article can be found online at https://doi.org/10.1016/j.heliyon.2024.e26442.

Appendix A

List of Symbols

Symbol	Description	Units
i	Chemical species index	–
c_i	Concentration of species i	mol/m^3

(continued on next page)

(*continued*)

Symbol	Description	Units
$c_{i,0}$	Initial concentration of species i	mol/m^3
a_i	Chemical activity of species i	–
d_f	Fiber diameter	m
d_p	Pore length	m
L	Cathode side length	m
D	Cathode thickness	m
S	Surface length	m
N	Total fibers number	–
ne	Number of electrons transferred	–
n_i	Number of fibers per side	–
N_i	Molar flow rate of species i	mol/s
D_i	Diffusion coefficient of species i	m^2/s
z_i	Electric charge number of species i	–
F	Faraday's constant (9.6485×10^4 C/mol)	C/mol
R	Molar gas constant [8.3145 J/(mol.K)]	J/(mol.K)
i	(Total) net current density	A/m^2
i_s	Current density at the electrode	A/m^2
i_l	Current density in the electrolyte	A/m^2
i_0	Exchange current density	A/m^2
i_{loc}	Local current density	A/m^2
T	Temperature	K
T_{ref}	Reference, or room temperature (25.0 °C)	K
p	Pressure	Pa
P_{ref}	Reference, or atmospheric pressure (1.0133 bar)	Pa
q	Volumetric flow rate	m^3/s
P_{in}	Inlet pressure	Pa
Q_{out}	Volumetric outflow rate	m^3/s
E_0	Standard equilibrium potential of reaction	V
E_{eq}	Equilibrium potential of reaction	V
E_c	Applied electric potential (vs. RHE)	V
pH	Electrolyte pH	–
u	Fluid surface velocity vector	m/s
$\vec{n}$	Outward unit normal vector	m/s
ν	Dynamic fluid viscosity	m^2/s
ε	Cathode porosity	–
σ_s	Electrode electric conductivity	S/m
σ_l	Electrolyte electric conductivity	S/m
α_c	Cathodic transfer coefficient	–
α_a	Anodic transfer coefficient	–
Φ	Ionic electric potential (vs. RHE)	V
Φ_s	Electrode electric potential (vs. RHE)	V
Φ_l	Electrolyte electric potential (vs. RHE)	V
η	Overvoltage (vs. RHE)	V
ρ	Electrolyte density	kg/m^3
μ	Electrolyte kinematic viscosity	kg/(m.s)
RHE	Reversible hydrogen electrode: $E_{H^+}^0\ V\ (vs.\ RHE) = E_{H^+}^0\ V\ (vs.\ SHE) - 0.059\ V\ pH$	V
SHE	Standard hydrogen electrode: $E_{H^+}^0\ V\ (vs.\ SHE) = 0\ V\ (at\ any\ temperature)$	V

References

[1] A.S. Reis Machado, M. Nunes da Ponte, CO2 capture and electrochemical conversion, Curr. Opin. Green Sustainable Chem. 11 (2018) 86–90, https://doi.org/10.1016/j.cogsc.2018.05.009.

[2] A.S.R. Machado, A.V.M. Nunes, M.N. da Ponte, Carbon dioxide utilization—electrochemical reduction to fuels and synthesis of polycarbonates, J. Supercrit. Fluids 134 (2018) 150–156, https://doi.org/10.1016/j.supflu.2017.12.023.

[3] S. Garg, M. Li, A.Z. Weber, L. Ge, L. Li, V. Rudolph, G. Wang, T.E. Rufford, Advances and challenges in electrochemical CO2 reduction processes: an engineering and design perspective looking beyond new catalyst materials, J. Mater. Chem. A 8 (2020) 1511–1544, https://doi.org/10.1039/C9TA13298H.

[4] H. Naims, Economics of carbon dioxide capture and utilization—a supply and demand perspective, Environ. Sci. Pollut. Res. 23 (2016) 22226–22241, https://doi.org/10.1007/s11356-016-6810-2.

[5] Global CCS Institute, The global status of CCS: 2015 summary report, Global CCS Institute (n.d.). https://www.globalccsinstitute.com/resources/publications-reports-research/the-global-status-of-ccs-2015-summary-report/(accessed July 5, 2023)..

[6] M.M. Halmann, Chemical Fixation of Carbon DioxideMethods for Recycling CO2 into Useful Products, CRC Press, Boca Raton, 1993, https://doi.org/10.1201/9781315139098.

[7] F. Vieira, B. Sarmento, A.S. Reis-Machado, J. Facão, M.J. Carvalho, M.J. Mendes, E. Fortunato, R. Martins, Prediction of sunlight-driven CO2 conversion: producing methane from photovoltaics, and full system design for single-house application, Mater. Today Energy 14 (2019) 100333, https://doi.org/10.1016/j.mtener.2019.07.004.

[8] A.C. Lourenço, A.S. Reis-Machado, E. Fortunato, R. Martins, M.J. Mendes, Sunlight-driven CO2-to-fuel conversion: exploring thermal and electrical coupling between photovoltaic and electrochemical systems for optimum solar-methane production, Mater. Today Energy 17 (2020) 100425, https://doi.org/10.1016/j.mtener.2020.100425.

[9] S. Messias, M.M. Sousa, M.N. da Ponte, C.M. Rangel, T. Pardal, A.S.R. Machado, Electrochemical production of syngas from CO2 at pressures up to 30 bar in electrolytes containing ionic liquid, React. Chem. Eng. 4 (2019) 1982–1990, https://doi.org/10.1039/C9RE00271E.

[10] T. Pardal, S. Messias, M. Sousa, A.S.R. Machado, C.M. Rangel, D. Nunes, J.V. Pinto, R. Martins, M.N. da Ponte, Syngas production by electrochemical CO2 reduction in an ionic liquid based-electrolyte, J. CO2 Util. 18 (2017) 62–72, https://doi.org/10.1016/j.jcou.2017.01.007.

[11] A. Al-Mamoori, A. Krishnamurthy, A.A. Rownaghi, F. Rezaei, Carbon capture and utilization update, Energy Technol. 5 (2017) 834–849, https://doi.org/10.1002/ente.201600747.

[12] S. Chu, A. Majumdar, Opportunities and challenges for a sustainable energy future, Nature 488 (2012) 294–303, https://doi.org/10.1038/nature11475.

[13] E.V. Kondratenko, G. Mul, J. Baltrusaitis, G.O. Larrazábal, J. Pérez-Ramírez, Status and perspectives of CO2 conversion into fuels and chemicals by catalytic, photocatalytic and electrocatalytic processes, Energy Environ. Sci. 6 (2013) 3112–3135, https://doi.org/10.1039/C3EE41272E.

[14] H.-R. "Molly" Jhong, S. Ma, P.J. Kenis, Electrochemical conversion of CO2 to useful chemicals: current status, remaining challenges, and future opportunities, Curr. Opin. Chem. Eng. 2 (2013) 191–199, https://doi.org/10.1016/j.coche.2013.03.005.

[15] M.A. Scibioh, B. Viswanathan, Chapter 9 - photoelectrochemical reduction of CO2, in: M.A. Scibioh, B. Viswanathan (Eds.), Carbon Dioxide to Chemicals and Fuels, Elsevier, 2018, pp. 437–474, https://doi.org/10.1016/B978-0-444-63996-7.00009-2.

[16] J. Albo, M. Alvarez-Guerra, A. Irabien, Electro-, photo-, and photoelectro-chemical reduction of CO2, in: Heterogeneous Catalysts, John Wiley & Sons, Ltd, 2021, pp. 649–669, https://doi.org/10.1002/9783527813599.ch36.

[17] A.S. Agarwal, Y. Zhai, D. Hill, N. Sridhar, The electrochemical reduction of carbon dioxide to formate/formic acid: engineering and economic feasibility, ChemSusChem 4 (2011) 1301–1310, https://doi.org/10.1002/cssc.201100220.

[18] O.S. Bushuyev, P.D. Luna, C.T. Dinh, L. Tao, G. Saur, J. van de Lagemaat, S.O. Kelley, E.H. Sargent, What should we make with CO2 and how can we make it? Joule 2 (2018) 825–832, https://doi.org/10.1016/j.joule.2017.09.003.

[19] D.R. Kauffman, J. Thakkar, R. Siva, C. Matranga, P.R. Ohodnicki, C. Zeng, R. Jin, Efficient electrochemical CO2 conversion powered by renewable energy, ACS Appl. Mater. Interfaces 7 (2015) 15626–15632, https://doi.org/10.1021/acsami.5b04393.

[20] R.J. Lim, M. Xie, M.A. Sk, J.-M. Lee, A. Fisher, X. Wang, K.H. Lim, A review on the electrochemical reduction of CO2 in fuel cells, metal electrodes and molecular catalysts, Catal. Today 233 (2014) 169–180, https://doi.org/10.1016/j.cattod.2013.11.037.

[21] J.A. Moya, N. Pardo, The potential for improvements in energy efficiency and CO2 emissions in the EU27 iron and steel industry under different payback periods, J. Clean. Prod. 52 (2013) 71–83, https://doi.org/10.1016/j.jclepro.2013.02.028.

[22] Twelve, Twelve | The Carbon Transformation Company, Twelve (n.d.). https://www.twelve.co/technology (accessed July 5, 2023)..

[23] I.S. Fernandes, Modelação de Cátodos Porosos para Redução Eletroquímica do CO2, masterThesis, 2022. https://run.unl.pt/handle/10362/132736 (accessed May 19, 2023).

[24] D. Antunes, Solar Fuels Design: Modeling Porous Cathodes for the Production of Carbon-Based Fuels from CO2, masterThesis, 2022. https://run.unl.pt/handle/10362/146926 (accessed May 19, 2023).

[25] CERT Systems, Our Technology, CERT Systems Inc, 2017. https://co2cert.com/about/cert-technology/ (accessed July 5, 2023).

[26] Evonik, Evonik and Siemens to generate high-value specialty chemicals from carbon dioxide and eco-electricity - Evonik Industries, Evonik (n.d.). https://corporate.evonik.com/en/media/press-releases/corporate/evonik-and-siemens-to-generate-high-value-specialty-chemicals-from-carbon-dioxide-and-eco-electricit-106259.html (accessed July 5, 2023)..

[27] Ecoparadigm, Our Mantra | Ecoparadigm | Ecoparadigm is inspired from the The Mobius Strip, Driving the Transition Towards a Resource-Efficient Future (n.d.). https://www.ecoparadigm.com/our-mantra (accessed July 5, 2023)..

[28] GDR Solar Fuels, Page D'accueil GDR Solar Fuels, GDR Solar Fuels, 2023. https://solarfuels.cnrs.fr/ (accessed March 16, 2023).

[29] E. Alper, O. Yuksel Orhan, CO2 utilization: developments in conversion processes, Petroleum 3 (2017) 109–126, https://doi.org/10.1016/j.petlm.2016.11.003.

[30] Y. Hori, H. Konishi, T. Futamura, A. Murata, O. Koga, H. Sakurai, K. Oguma, "Deactivation of copper electrode" in electrochemical reduction of CO2, Electrochim. Acta 50 (2005) 5354–5369, https://doi.org/10.1016/j.electacta.2005.03.015.

[31] A. Wuttig, Y. Surendranath, Impurity ion complexation enhances carbon dioxide reduction catalysis, ACS Catal. 5 (2015) 4479–4484, https://doi.org/10.1021/acscatal.5b00808.

[32] B. Jermann, J. Augustynski, Long-term activation of the copper cathode in the course of CO2 reduction, Electrochim. Acta 39 (1994) 1891–1896, https://doi.org/10.1016/0013-4686(94)85181-6.

[33] G. Nogami, H. Itagaki, R. Shiratsuchi, Pulsed electroreduction of CO 2 on copper electrodes-II, J. Electrochem. Soc. 141 (1994) 1138, https://doi.org/10.1149/1.2054886.

[34] J. Yano, T. Morita, K. Shimano, Y. Nagami, S. Yamasaki, Selective ethylene formation by pulse-mode electrochemical reduction of carbon dioxide using copper and copper-oxide electrodes, J. Solid State Electrochem. 11 (2007) 554–557, https://doi.org/10.1007/s10008-006-0181-4.

[35] J. Yano, S. Yamasaki, Pulse-mode electrochemical reduction of carbon dioxide using copper and copper oxide electrodes for selective ethylene formation, J. Appl. Electrochem. 38 (2008) 1721–1726, https://doi.org/10.1007/s10800-008-9622-3.

[36] P. Kedzierzawski, J. Augustynski, Poisoning and activation of the gold cathode during electroreduction of CO 2, J. Electrochem. Soc. 141 (1994) L58, https://doi.org/10.1149/1.2054936.

[37] B. Kumar, J.P. Brian, V. Atla, S. Kumari, K.A. Bertram, R.T. White, J.M. Spurgeon, Controlling the product syngas H2:CO ratio through pulsed-bias electrochemical reduction of CO2 on copper, ACS Catal. 6 (2016) 4739–4745, https://doi.org/10.1021/acscatal.6b00857.

[38] L.M. Chiacchiarelli, Y. Zhai, G.S. Frankel, A.S. Agarwal, N. Sridhar, Cathodic degradation mechanisms of pure Sn electrocatalyst in a nitrogen atmosphere, J. Appl. Electrochem. 42 (2012) 21–29, https://doi.org/10.1007/s10800-011-0367-z.

[39] M.N. Mahmood, D. Masheder, C.J. Harty, Use of gas-diffusion electrodes for high-rate electrochemical reduction of carbon dioxide. I. Reduction at lead, indium- and tin-impregnated electrodes, J. Appl. Electrochem. 17 (1987) 1159–1170, https://doi.org/10.1007/BF01023599.

[40] C.-T. Dinh, T. Burdyny, M.G. Kibria, A. Seifitokaldani, C.M. Gabardo, F.P. García de Arquer, A. Kiani, J.P. Edwards, P. De Luna, O.S. Bushuyev, C. Zou, R. Quintero-Bermudez, Y. Pang, D. Sinton, E.H. Sargent, CO2 electroreduction to ethylene via hydroxide-mediated copper catalysis at an abrupt interface, Science 360 (2018) 783–787, https://doi.org/10.1126/science.aas9100.

[41] K. Wu, E. Birgersson, B. Kim, P.J.A. Kenis, I.A. Karimi, Modeling and experimental validation of electrochemical reduction of CO2 to CO in a microfluidic cell, J. Electrochem. Soc. 162 (2014) F23, https://doi.org/10.1149/2.1021414jes.

[42] J.-P. Jones, G.K.S. Prakash, G.A. Olah, Electrochemical CO2 reduction: recent advances and current trends, Isr. J. Chem. 54 (2014) 1451–1466, https://doi.org/10.1002/ijch.201400081.

[43] O. Aschenbrenner, P. Styring, Comparative study of solvent properties for carbon dioxide absorption, Energy Environ. Sci. 3 (2010) 1106–1113, https://doi.org/10.1039/C002915G.

[44] T. Saeki, K. Hashimoto, N. Kimura, K. Omata, A. Fujishima, Electrochemical reduction of CO2 with high current density in a CO2 + methanol medium at various metal electrodes, J. Electroanal. Chem. 404 (1996) 299–302, https://doi.org/10.1016/0022-0728(95)04374-8.

[45] K. Hara, A. Tsuneto, A. Kudo, T. Sakata, Electrochemical reduction of CO2 on a Cu electrode under high pressure: factors that determine the product selectivity, J. Electrochem. Soc. 141 (1994) 2097, https://doi.org/10.1149/1.2055067.

[46] M. Todoroki, K. Hara, A. Kudo, T. Sakata, Electrochemical reduction of high pressure CO2 at Pb, Hg and in electrodes in an aqueous KHCO3 solution, J. Electroanal. Chem. 394 (1995) 199–203, https://doi.org/10.1016/0022-0728(95)04010-L.

[47] M. Heßelmann, B.C. Bräsel, R.G. Keller, M. Wessling, Simulation-based guidance for improving CO2 reduction on silver gas diffusion electrodes, Electrochem. Sci. Adv. 3 (2023) 2100160, https://doi.org/10.1002/elsa.202100160.

[48] O.A. El-Shafie, R.M. El-Maghraby, J. Albo, S.-E.K. Fateen, A. Abdelghany, Modeling and numerical investigation of the performance of gas diffusion electrodes for the electrochemical reduction of carbon dioxide to methanol, Ind. Eng. Chem. Res. 59 (2020) 20929–20942, https://doi.org/10.1021/acs.iecr.0c02358.

[49] A.R.T. Morrison, V. van Beusekom, M. Ramdin, L.J.P. van den Broeke, T.J.H. Vlugt, W. de Jong, Modeling the electrochemical conversion of carbon dioxide to formic acid or formate at elevated pressures, J. Electrochem. Soc. 166 (2019) E77, https://doi.org/10.1149/2.0121904jes.

[50] C. Delacourt, J. Newman, Mathematical modeling of CO2 reduction to CO in aqueous electrolytes: II. Study of an electrolysis cell making syngas from and reduction at room temperature, J. Electrochem. Soc. 157 (2010) B1911, https://doi.org/10.1149/1.3502533.

[51] C. Georgopoulou, S. Jain, A. Agarwal, E. Rode, G. Dimopoulos, N. Sridhar, N. Kakalis, On the modelling of multidisciplinary electrochemical systems with application on the electrochemical conversion of CO2 to formate/formic acid, Comput. Chem. Eng. 93 (2016) 160–170, https://doi.org/10.1016/j.compchemeng.2016.06.012.

[52] L.-C. Weng, A.T. Bell, A.Z. Weber, Towards membrane-electrode assembly systems for CO2 reduction: a modeling study, Energy Environ. Sci. 12 (2019) 1950–1968, https://doi.org/10.1039/C9EE00909D.

[53] L.C. Brée, M. Wessling, A. Mitsos, Modular modeling of electrochemical reactors: comparison of CO2-electolyzers, Comput. Chem. Eng. 139 (2020) 106890, https://doi.org/10.1016/j.compchemeng.2020.106890.

[54] Y.C. Tan, K.B. Lee, H. Song, J. Oh, Modulating local CO2 concentration as a general strategy for enhancing C−C coupling in CO2 electroreduction, Joule 4 (2020) 1104–1120, https://doi.org/10.1016/j.joule.2020.03.013.

[55] D.G. Wheeler, B.A.W. Mowbray, A. Reyes, F. Habibzadeh, J. He, C.P. Berlinguette, Quantification of water transport in a CO2 electrolyzer, Energy Environ. Sci. 13 (2020) 5126–5134, https://doi.org/10.1039/D0EE02219E.

[56] J.W. Blake, J.T. Padding, J.W. Haverkort, Analytical modelling of CO2 reduction in gas-diffusion electrode catalyst layers, Electrochim. Acta 393 (2021) 138987, https://doi.org/10.1016/j.electacta.2021.138987.

[57] R. Kas, A.G. Star, K. Yang, T. Van Cleve, K.C. Neyerlin, W.A. Smith, Along the channel gradients impact on the spatioactivity of gas diffusion electrodes at high conversions during CO2 electroreduction, ACS Sustain. Chem. Eng. 9 (2021) 1286–1296, https://doi.org/10.1021/acssuschemeng.0c07694.

[58] J.R. Hudkins, D.G. Wheeler, B. Peña, C.P. Berlinguette, Rapid prototyping of electrolyzer flow field plates, Energy Environ. Sci. 9 (2016) 3417–3423, https://doi.org/10.1039/C6EE01997H.

[59] J. Pérez-Ramírez, N. López, Strategies to break linear scaling relationships, Nat. Catal. 2 (2019) 971–976, https://doi.org/10.1038/s41929-019-0376-6.

[60] S. Pablo-García, R. García-Muelas, A. Sabadell-Rendón, N. López, Dimensionality reduction of complex reaction networks in heterogeneous catalysis: from linear-scaling relationships to statistical learning techniques, WIREs Comput. Mol. Sci. 11 (2021) e1540, https://doi.org/10.1002/wcms.1540.

[61] F. Dattila, R.R. Seemakurthi, Y. Zhou, N. López, Modeling Operando electrochemical CO2 reduction, Chem. Rev. 122 (2022) 11085–11130, https://doi.org/10.1021/acs.chemrev.1c00690.

[62] A. Vojvodic, J.K. Nørskov, New design paradigm for heterogeneous catalysts, Natl. Sci. Rev. 2 (2015) 140–143, https://doi.org/10.1093/nsr/nwv023.

[63] M.R. Singh, Y. Kwon, Y. Lum, J.W.I. Ager, A.T. Bell, Hydrolysis of electrolyte cations enhances the electrochemical reduction of CO2 over Ag and Cu, J. Am. Chem. Soc. 138 (2016) 13006–13012, https://doi.org/10.1021/jacs.6b07612.

[64] F.L.P. Veenstra, N. Ackerl, A.J. Martín, J. Pérez-Ramírez, Laser-microstructured copper reveals selectivity patterns in the electrocatalytic reduction of CO2, Chem 6 (2020) 1707–1722, https://doi.org/10.1016/j.chempr.2020.04.001.

[65] J. Rosen, G.S. Hutchings, Q. Lu, S. Rivera, Y. Zhou, D.G. Vlachos, F. Jiao, Mechanistic insights into the electrochemical reduction of CO2 to CO on nanostructured Ag surfaces, ACS Catal. 5 (2015) 4293–4299, https://doi.org/10.1021/acscatal.5b00840.

[66] M. Ma, B.J. Trześniewski, J. Xie, W.A. Smith, Selective and efficient reduction of carbon dioxide to carbon monoxide on oxide-derived nanostructured silver electrocatalysts, Angew. Chem. Int. Ed. 55 (2016) 9748–9752, https://doi.org/10.1002/anie.201604654.

[67] M.R. Singh, J.D. Goodpaster, A.Z. Weber, M. Head-Gordon, A.T. Bell, Mechanistic insights into electrochemical reduction of CO2 over Ag using density functional theory and transport models, Proc. Natl. Acad. Sci. USA 114 (2017) E8812–E8821, https://doi.org/10.1073/pnas.1713164114.

[68] S. Messias, M. Nunes da Ponte, A.S. Reis-Machado, Carbon Materials as Cathode Constituents for Electrochemical CO2 Reduction—A Review, C 5, 2019, p. 83, https://doi.org/10.3390/c5040083.

[69] W. Luo, J. Zhang, M. Li, A. Züttel, Boosting CO production in electrocatalytic CO2 reduction on highly porous Zn catalysts, ACS Catal. 9 (2019) 3783–3791, https://doi.org/10.1021/acscatal.8b05109.

[70] C. Ma, X. Li, L. Lin, L. Chen, M. Wang, J. Zhou, A two-dimensional porous electrode model for designing pore structure in a quinone-based flow cell, J. Energy Storage 18 (2018) 16–25, https://doi.org/10.1016/j.est.2018.04.007.

[71] Mumps Technologies SAS, MUMPS: a parallel sparse direct solver, MUMPS: MUltifrontal Massively Parallel Sparse Direct Solver (n.d.). https://mumps-solver.org/index.php (accessed May 27, 2023)..

[72] COMSOL Multiphysics, Understanding and Changing the Element Order, COMSOL Multiphysics (n.d.). https://www.comsol.com/support/learning-center/article/Understanding-and-Changing-the-Element-Order-59391 (accessed May 27, 2023)..

[73] A. Guedes, M.J. Mendes, P.P. Freitas, J.L. Martins, Study of synthetic ferrimagnet-synthetic antiferromagnet structures for magnetic sensor application, J. Appl. Phys. 99 (2006) 08B703, https://doi.org/10.1063/1.2162817.

[74] COMSOL Multiphysics, The Segregated Solver, COMSOL Documentation (n.d.). https://doc.comsol.com/5.5/doc/com.comsol.help.comsol/comsol_ref_solver.27.127.html#1053564 (accessed May 27, 2023)..

[75] M.J. Mendes, H.K. Schmidt, M. Pasquali, Brownian dynamics simulations of single-wall carbon nanotube separation by type using dielectrophoresis, J. Phys. Chem. B 112 (2008) 7467–7477, https://doi.org/10.1021/jp711450w.

[76] COMSOL Multiphysics, The Nelder–Mead Solver, COMSOL Documentation (n.d.). https://doc.comsol.com/6.1/docserver/#!/com.comsol.help.opt/opt_ug_solver.8.12.html (accessed May 28, 2023)..

[77] G.A. Zampogna, A. Bottaro, Fluid flow over and through a regular bundle of rigid fibres, J. Fluid Mech. 792 (2016) 5–35, https://doi.org/10.1017/jfm.2016.66.

[78] W.H. Zhong, I.G. Currie, D.F. James, Creeping flow through a model fibrous porous medium, Exp. Fluid 40 (2006) 119–126, https://doi.org/10.1007/s00348-005-0053-1.

[79] A. Desalvo, P. Gondi, F.A. Levi, F. Zignani, Electrical conductivity of high-purity zinc, Nuovo Cim 31 (1964) 904–913, https://doi.org/10.1007/BF02733804.

[80] S. Nitopi, E. Bertheussen, S.B. Scott, X. Liu, A.K. Engstfeld, S. Horch, B. Seger, I.E.L. Stephens, K. Chan, C. Hahn, J.K. Nørskov, T.F. Jaramillo, I. Chorkendorff, Progress and perspectives of electrochemical CO2 reduction on copper in aqueous electrolyte, Chem. Rev. 119 (2019) 7610–7672, https://doi.org/10.1021/acs.chemrev.8b00705.

[81] R. Chang, K. Goldsby, Chemistry, twelfth ed., McGraw-Hill Education, 2015.

[82] A. Bharti, R. Natarajan, Chapter 7 - proton exchange membrane testing and diagnostics, in: G. Kaur (Ed.), PEM Fuel Cells, Elsevier, 2022, pp. 137–171, https://doi.org/10.1016/B978-0-12-823708-3.00007-9.

[83] E.L. Cussler, Diffusion: Mass Transfer in Fluid Systems, Cambridge University Press, 1997.

[84] G. Bisweswar, A. Al-Hamairi, S. Jin, Carbonated water injection: an efficient EOR approach. A review of fundamentals and prospects, J. Pet. Explor. Prod. Technol. 10 (2020) 673–685, https://doi.org/10.1007/s13202-019-0738-2.